Evaluating the Benefits of Kinetic Monte Carlo and Microkinetic Modeling for Catalyst Design Studies in the Presence of Lateral Interactions

*Xiao Li and Lars C. Grabow**

William A. Brookshire Department of Chemical and Biomolecular Engineering, University of Houston, Houston, TX 77204-4004, USA

*grabow@uh.edu

Abstract

Popular computational catalyst design strategies rely on the identification of reactivity descriptors, which can be used along with Brønsted−Evans−Polanyi (BEP) and scaling relations as input to a microkinetic model (MKM) to make predictions for activity or selectivity trends. The main benefit of this approach is related to the inherent dimensionality reduction of the large material space to just a few catalyst descriptors. Conversely, it is well documented that a small set of descriptors is insufficient to capture the intricacies and complexities of a real catalytic system. The inclusion of coverage effects through lateral adsorbate-adsorbate interactions can narrow the gap between simplified descriptor predictions and real systems, but mean-field MKMs cannot properly account for local coverage effects. This shortcoming of the mean-field approximation can be rectified by switching to a lattice-based kinetic Monte Carlo (kMC) method using cluster expansion representation of adsorbate−adsorbate lateral interactions.

Using the prototypical CO oxidation reaction as an example, we critically evaluate the benefits of kMC over MKM in terms of trend predictions and computational cost when using only a small set of input parameters. After confirming that in the absence of lateral interactions the kMC and MKM approaches yield identical trends and mechanistic information, we observed substantial differences between the two kinetic models when lateral interactions were introduced. The mean-field implementation applies coverage corrections directly to the descriptors, causing an artificial overprediction of the activity of strongly binding metals. In contrast, the cluster expansion in kMC implementation can differentiate among the highly active metals but it is very sensitive to the set of included interaction parameters. Considering that computational screening relies on a minimal set of descriptors, for which MKM makes reasonable trend predictions at a ca. three orders of magnitude lower computational cost than kMC, the MKM approach does provide a better entry point for computational catalyst design.

Keywords: Catalyst design, coverage effects, kinetic Monte Carlo, microkinetic modeling, CO oxidation

1. Introduction

Microkinetic modeling (MKM) is a powerful tool for relating reaction mechanistic insight to overall observable rates under various reaction conditions; it is extensively used in catalyst, reactor and process design because it is easy to implement and only requires solving a system of coupled ordinary differential equations (ODEs) [1,2]. In addition to the reaction conditions (T, P_i), the ODEs contain a pair of rate coefficients for all elementary steps, causing the number of parameters to quickly increase with mechanistic complexity. But when employed in conjunction with Brønsted−Evans−Polanyi (BEP) and scaling relationships based on catalytic descriptors, the complexity of the MKM can be reduced, allowing the study of activity and selectivity trends across large material spaces [3–9]. Optimal catalysts for a given set of reaction conditions are located near the top of the resulting volcano curve in descriptor space. The underlying mean-field approximation in MKM simplifies the mathematical description of the problem but disregards the spatial distribution of adsorbates on a catalyst surface. This limitation can be a concern when multifunctional catalysts with interacting sites of different types are studied, for instance at the interface between a metal particle and oxide support [10–12]. In such cases, diffusion between the distinct sites must be explicitly considered. Another example is the formation of ordered overlayers or islands, resulting from attractive interactions, particularly when surface diffusion is slow. While lateral interactions can be approximated in the MKM approach by referencing the average surface coverage, this solution only provides a correction term for energies and does not capture deviations from the law of mass action [13–15]. To explicitly consider correlations, fluctuations, and spatial distributions of surface species, the most common approach is based on solving the Markovian master equation within a kinetic Monte Carlo (kMC) simulation [16,17].

A convenient formalism for expressing lateral interactions on a 2D lattice is the cluster expansion Hamiltonian, which can incorporate short-range, long-range, and multibody interactions [18,19]. To take advantage of the explicit treatment of lateral adsorbate interactions for both energy corrections and non-uniform adsorbate distributions, the kMC model requires additional input information, which is usually obtained from computationally demanding density functional theory (DFT) calculations, in addition to the higher computational expense for solving the Markovian master equation.

Hoffmann and Bligaard [20] developed a lattice kMC solver specifically designed for descriptor-based catalyst screening studies and showed that in the absence of surface diffusion limitations and adsorbate-adsorbate interactions MKM and kMC approaches yield identical trends. They inferred that if lateral interactions or diffusion limitations were present, significant differences between MKM and kMC are expected. To properly evaluate the practical advantages of MKM and kMC in terms of efficiency and accuracy in the context of descriptor-based catalyst design particularly in the presence of lateral interactions, we studied the prototypical CO oxidation reaction on close-packed fcc(111) surfaces, for which MKM-based trend studies with and without lateral interactions have been published. In particular, we refer to the screening studies published by Falsig *et al.* [21] and Grabow *et al.* [13], who reported BEP relations, scaling relationships, and lateral interaction parameters for adsorbate-adsorbate interactions, respectively. Using the same mechanistic assumptions and rate constants, we focus on the corresponding kMC simulations and juxtapose both approaches in terms of their accurate capture of relevant physical phenomena, performance, practical implementation, and computational cost.

2. Methods

Following prior work [13,21], we consider the following five elementary reactions:

$$CO(g) + * \rightleftharpoons CO^* \quad \text{(R1)}$$

$$O_2(g) + * \rightleftharpoons O_2^* \quad \text{(R2)}$$

$$O_2^* + * \rightleftharpoons 2O^* \quad \text{(R3)}$$

$$CO^* + O^* \rightleftharpoons CO_2(g) + 2* \quad \text{(R4)}$$

$$CO^* + O_2^* \rightleftharpoons CO_2(g) + O^* + * \quad \text{(R5)}$$

To capture the effects of surface diffusion in the grid-based lattice kMC simulation we must also add three diffusion steps, R6–R8,

$$CO^* + * \rightleftharpoons * + CO^* \quad \text{(R6)}$$

$$O^* + * \rightleftharpoons * + O^* \quad \text{(R7)}$$

$$O_2^* + * \rightleftharpoons * + O_2^* \quad \text{(R8)}$$

We assume that the molecular adsorption steps for CO and O_2 are non-activated and their adsorption rate constants can be estimated from collision theory with the sticking coefficient approximated as unity [22].

$$k_{ads} = P_x \cdot \frac{A_{st}}{\sqrt{2\pi m_x k_B T}} \quad \text{Eq. (1)}$$

In Eq. (1), A_{st} is the effective area of the sites where the reactions occur, m_x is the molecular weight of the species x, k_B is the Boltzmann constant, T is the temperature, and P_x is the partial pressure of species x. The rate constants of the surface reactions and diffusions (R3–R8) were obtained from transition state theory [23] according to Eq. (2),

$$k_{rxn} = \frac{k_B T}{h} \cdot e^{\frac{\Delta S^{\ddagger}}{k_B}} \cdot e^{-\frac{\Delta {E_a}^{\ddagger}}{k_B T}} \quad \text{Eq. (2)}$$

where $\Delta {E_a}^{\ddagger} = E_{TS} - E_{IS}$ is the activation energy. Transition state energies, E_{TS}, of R3, R4, and R5 and the binding energy E_{O_2} of O_2* are determined by reported scaling relations [13,21]

$$E_{TS,R3} = 1.387\, E_O + 1.5793 \text{ eV} \quad \text{Eq. (3)}$$

$$E_{TS,R4} = 0.6997\, (E_O + E_{CO}) + 0.0417 \text{ eV} \quad \text{Eq. (4)}$$

$$E_{TS,R5} = 0.81018\, (E_O + E_{CO}) - 0.058559 \text{ eV} \quad \text{Eq. (5)}$$

$$E_{O_2} = 0.8925\, E_O + 0.2159 \text{ eV} \quad \text{Eq. (6)}$$

where E_O is the binding energy of O* and E_{CO} is the binding energy of CO*. The activation barriers for diffusion steps R6, R7, and R8 are obtained from a linear correlation between the activation barrier and the initial-state energy BE_{IS} [24].

$$\Delta {E_a}^{\ddagger} = -0.12\, BE_{IS} - 0.02 \text{ eV} \quad \text{Eq. (7)}$$

We ensured thermodynamic consistency by calculating the reverse rate constant k_i^- from the forward rate constant k_i^+ and the equilibrium constant K_i as $k_i^- = \frac{k_i^+}{K_i}$ for each elementary step. The entropies for the gas species are $S_{CO} = 197.66\,\mathrm{J \cdot K^{-1} \cdot mol^{-1}}$, $S_{CO_2} = 213.74\,\mathrm{J \cdot K^{-1} \cdot mol^{-1}}$, and $S_{O_2} = 205\,\mathrm{J \cdot K^{-1} \cdot mol^{-1}}$. The entropy for all surface species is assumed to be zero.

Instead of solving the system of coupled ordinary differential equations numerically, we obtained the mean-field solution from the analytical rate expression derived in reference [21]. In their derivation, Falsig *et al.* assumed the non-activated molecular adsorption of CO and O_2 to be quasi-equilibrated. Our kMC simulations were performed in the Graph-Theoretical kinetic Monte Carlo (GT-kMC) framework as implemented in the software package Zacros [25,26] on a hexagonal lattice of 50 × 50 points. Details on the inclusion of lateral interactions in both kinetic models along with the MKM code and kMC input files are provided in the SI.

To compare the reactivity trends of CO oxidation qualitatively between MKM and kMC implementations, we use a normalized turnover frequency (TOF) under steady-state conditions at each grid point of the descriptor space. For the kMC model the TOF is extracted as the slope of the number of CO_2 molecules produced as a function of time, after steady state has been reached. The normalized TOF is then defined as

$$TOF_{normalized} = \frac{\log(TOF) - \log(TOF_{min})}{\log(TOF_{max}) - \log(TOF_{min})} \qquad \text{Eq. (8)}$$

where TOF_{min} and TOF_{max} represent the minimum TOF and maximum TOF, respectively, within the descriptor space.

3. Results and Discussion

3.1 Reactivity Trends in the Absence of Lateral Interactions

The computational time requirements of the kMC simulation depend strongly on the stiffness of the reaction equations and number of lateral interactions included in the model. But even in the absence of lateral interactions, kMC simulations are very slow to converge to steady-state. For instance, in our simple CO oxidation model the computational requirements are about 3 orders of magnitude higher compared to the MKM implementation. Thus, we initialized our kMC simulations with the steady-state coverage calculated from the MKM run at each grid point to reduce the time to convergence. The resulting CO oxidation activity map in the absence of adsorbate–adsorbate interactions is plotted as a function of the two independent variables E_O and E_{CO} in Figure 1. Because of the higher computational cost, we employ a smaller descriptor range around the peak position compared with other descriptor-based volcanoes published by Falsig *et al.*[21] and Grabow *et al.* [13]. The comparison of the MKM results (Figure 1a) and kMC results (Figure 1c) show that the position of the top of the volcano marked with a star at (-1.0, -1.3) is identical in both cases. Moreover, the kMC results (Figure 1c) reproduce the surface coverage from MKM (Figure 1a) and a snapshot of the lattice configuration at steady state is shown in Figure S1. For both models oxygen is the most abundant surface intermediate when E_O is strongly negative, i.e. strong binding of oxygen. As the oxygen binding energy becomes weaker, CO* becomes the dominant adsorbate on the surface. The coverage of O_2* is always less than 2×10^{-5} monolayer (ML) and is omitted in Figure 1.

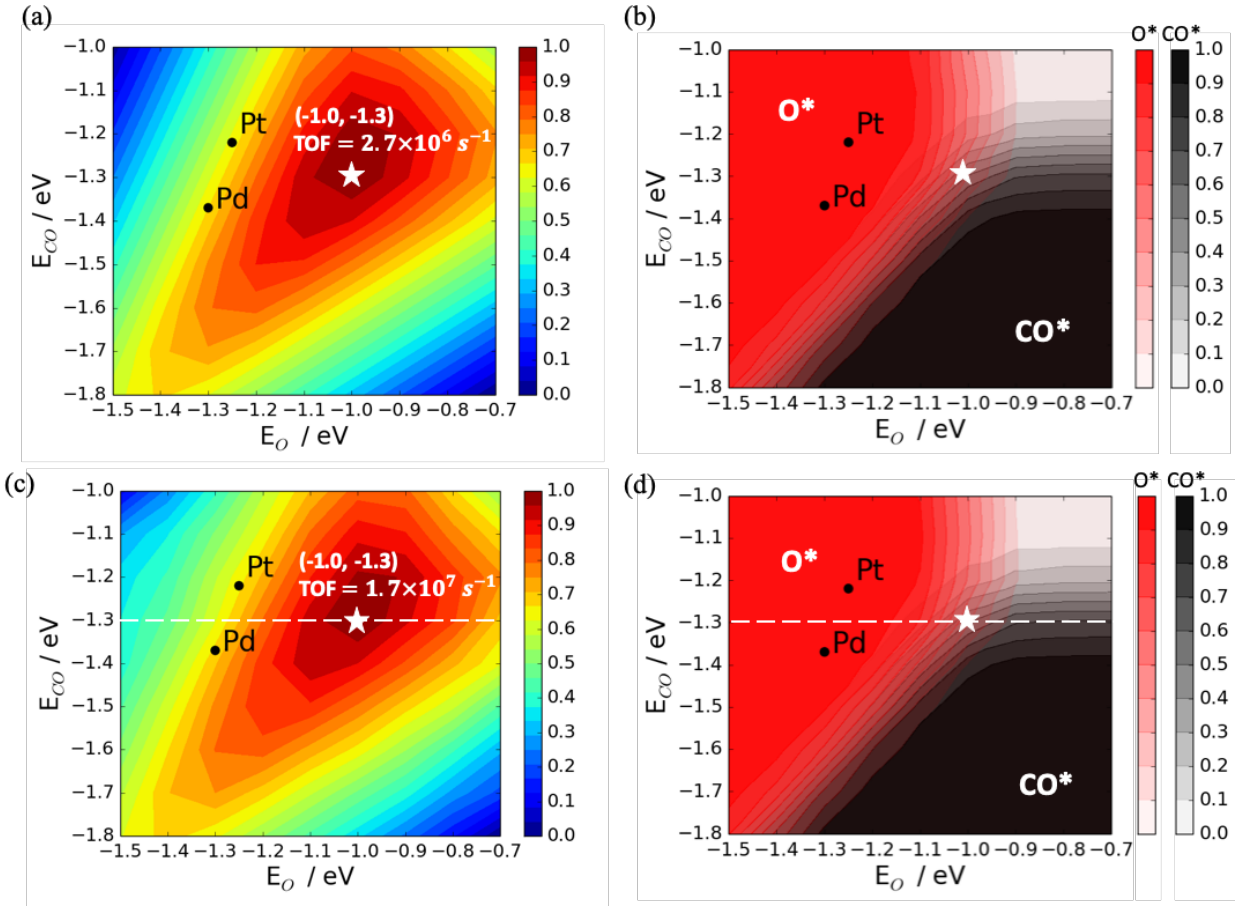

Figure 1: Comparison of trend predictions for CO oxidation as a function of E_O and E_{CO} from MKM (a, b) and kMC (c, d) models at $T = 600\,K$, $P_{O_2} = 0.33\,bar$, $P_{CO_2} = 1.0\,bar$, $P_{co} = 0.67\,bar$ in the absence of lateral interactions. The normalized TOF is shown in contour plots obtained from (a) MKM and (c) kMC. The corresponding surface coverages of O* (red) and CO* (black) are provided in panels (b) for MKM and (d) for kMC. The star marks the point of maximum activity and the corresponding coordinates in descriptor space are provided in parentheses. The color depth in (b) and (d) is linearly correlated with the coverage. The coverage of O_2* is always $< 2 \times 10^{-5}$ ML and is not shown. The horizontal dashed line in panels (c) and (d) represents a fixed value of $E_{CO} = -1.3\,eV$ used in the degree of rate control analysis in the kMC model.

Given the identical list of elementary reaction steps, rate constants and reaction conditions we expected the TOF of the MKM and kMC simulation to be identical; however, we found that the absolute TOF from kMC was nearly one order of magnitude higher than from MKM. Since it has been proven that the chemical master equations for on-lattice stochastic systems reduces to the well-mixed case in the limit of fast diffusion [27], we analyzed the sensitivity of the kMC model with respect to the diffusion barriers of steps R6–R8, but did not observe any notable differences. Moreover, under steady-state conditions at the top of the volcano we calculate the probability of finding an O* or O_2* species next to CO* as $\frac{Total\ number\ of\ CO*-O*\ and\ CO*-O_2*\ pairs}{Total\ number\ of\ active\ sites \times 6 \times 2} = 0.157$,

which is in good agreement with the value of $[CO*][O*] + [CO*][O_2*] = 0.151$ obtained from the law of mass action in the mean-field approximation. The value of 6 in the denominator of the above equation represents the number of nearest neighbor sites for each active site and value of 2 is needed to eliminate double counting. Hence, we may conclude that the surface species in our kMC run are well-mixed within reasonably small error bars.

Similar discrepancies between the TOF calculated with MKM and kMC have been reported by a number of other authors, for example, Temel *et al*. [28], Andersen *et al*. [29] and Hoffmann *et al*. [20]. All studies found that the TOF discrepancy can be caused by different probabilities of finding reactant pairs, even when diffusion is fast. For instance, the dissociative adsorption of O_2 requires two adjacent vacant sites, while a single site suffices for CO adsorption, potentially causing heterogeneities in the surface adlayer. In our case, R5 allows O_2* to directly react with CO*, which eliminates the need for adjacent vacant sites for O_2 activation even when CO* is the most abundant surface intermediate. Hoffmann and Bligaard tested a number of additional strategies, such as embedding mean-field boundary conditions, disabling diffusion steps and desorption steps for low-coverage regions, employing geometry factors, and steady-state detection techniques, but were still unable to exactly match the TOF values from MKM and kMC models [20]. Given the challenges to obtain identical TOF values and the fact that absolute TOF values are practically meaningless for trend studies, we chose to normalize the TOF when we compare trend predictions across the descriptor domain obtained from MKM and kMC approaches.

A common form of sensitivity analysis for kinetic models is known as Campbell's degree of rate control which aides in the identification of rate-determining steps and investigation of reaction mechanisms [30,31].

$$X_{rc,i} = \frac{k_i}{r}\left(\frac{\partial r}{\partial k_i}\right)_{K_i, k_{j\neq i}} \approx \frac{k_i^0}{r^0} \times \frac{r - r^0}{k_i - k_i^0} = \frac{r - r^0}{x \times r^0} \qquad \text{Eq. (9)}$$

This analysis is straight forward to implement by approximating the partial derivative as finite difference. Here, x denotes the step size relative to the reference rate constant k_i^0 of each elementary step, i.e., $k_i = (1 + x)\ k_i^0$ and the corresponding rate at the reference condition is denoted as r^0. All equilibrium constants K_i and rate constants $k_{j\neq i}$ of all other reaction steps remain unchanged.

Our X_{rc} analysis using the MKM approach and $x = 0.1$ over the descriptor space is presented in Figure 2. Since we assumed that the adsorption of O_2 and CO is quasi-equilibrated, these steps are not considered in the X_{rc} analysis. A large value of X_{rc} for any reaction step *i* implies that the overall reaction rate has a high degree of sensitivity to the rate-determining transition state of step *i*. We find the largest X_{rc} values for steps R4 and R5, while $X_{rc,R3}$ is essentially zero everywhere. This observation is consistent with the fact that the reaction rate of O_2* dissociation is nearly zero across all simulations and the entire descriptor space. Thus, the dominant reaction pathway proceeds via the sequence of R5 ($CO^* + O_2^* \rightleftharpoons CO_2(g) + O^* + *$) followed by the reaction of O* with a second CO* in step R4 ($CO^* + O^* \rightleftharpoons CO_2(g) + 2*$). At steady state, CO* oxidation with O* (R4) and O_2* (R5) have the same reaction rate.

In the O*-covered region identified in Figure 1(c) we find R4 to be rate-determining with $X_{rc,R4} \approx 2$, while R5 is rate-determining elsewhere. This shift between rate-determining steps is clearly visible in Figure 2. Interestingly, we also find a negative value for $X_{rc,R5}$ in the O*-covered region, indicating that fast CO* oxidation with O_2* lowers the overall reaction rate here. To explain

the combination of $X_{rc,R4} \approx 2$ and $X_{rc,R5} \approx -1$ in the O*-poisoned region, we note that R4 is necessary to remove O* as CO_2 and to regenerate two empty sites. The two empty sites are rapidly occupied by adsorbing CO* and O_2*, leading to the formation of another CO_2 molecule and restoring the poisoning O*. Hence, accelerating R4 accelerates the formation of two CO_2 molecules, which explains the value of $X_{rc,R4} \approx 2$. The negative value of $X_{rc,R5}$ is a result of step R5 producing more O* when the surface is already saturated with O* and inhibiting the adsorption of more CO*. The interplay between steps R4 and R5 is ultimately determined by their respective rate constants. Since the transition state energy of step R5 is already lower than that of R4, a further increase in the rate of R5 forces more flux through step R4. Conversely, when the O* coverage is low, CO* oxidation with O* is quasi-equilibrated with $X_{rc,R4} \approx 0$ and the single rate-determining step is O* formation by the reaction of O_2* with CO*.

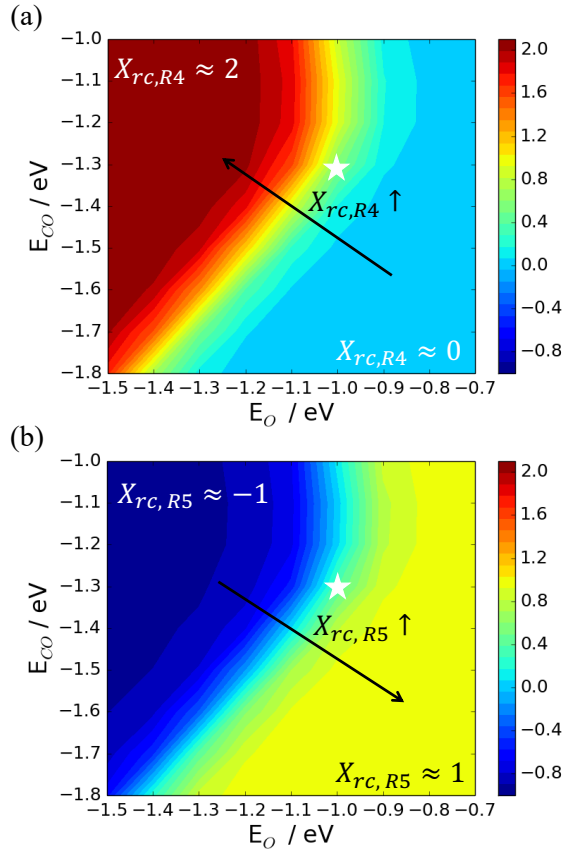

Figure 2: Degree of rate control (X_{rc}) for significant reaction steps (a) R4 and (b) R5 during CO oxidation in the absence of lateral interactions from the MKM model at $T = 600\,K$, $P_{O_2} = 0.33\,bar$, $P_{CO_2} = 1.0\,bar$, $P_{co} = 0.67\,bar$. The star marks the point of maximum activity.

Extracting the dominant reaction pathway from a kMC simulation is most easily accomplished by examining the frequency of individual reaction events. Figure 3 shows such an event frequency graph at the point of maximum TOF in the descriptor space. The information in Figure 3 is fully consistent with the results from the MKM model: the adsorption of CO and O_2 (R1, R2) are quasi-equilibrated; O_2 dissociation (R3) has no contribution; steps R4 and R5 are irreversible; and the net reaction rate of R4 is equal to the reaction rate of R5. Moreover, the

diffusion of CO* and O* is very fast, and the low frequency of O_2* diffusion steps is attributed to the very low coverage of O_2*. While the mechanistic interpretation of the event frequency graph is rather intuitive, it does not provide enough information to pinpoint the rate determining step between R4 and R5.

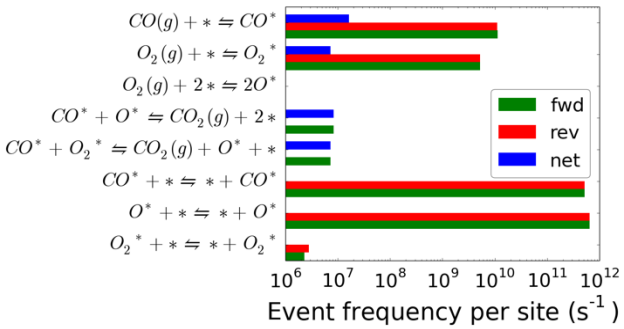

Figure 3: Event frequency for each elementary step at steady state in the absence of interactions from kMC simulations with E_O = -1.0 eV and E_{CO} = -1.3 eV, corresponding to the point of maximum activity.

Mathematically the degree of rate control can be obtained from any kinetic model, but the stochastic nature of the kMC algorithm introduces a large amount of noise when finite differences are taken. To address this issue, Hess *et al.* [32] have proposed to use a rather large step size (x = 1.0) and average the value of X_{rc} over three simulations. We followed this approach and initialized each of the three simulation with changed rate constants with the same steady-state coverage obtained from the simulation using the reference rate constants k_i^0, but the adsorbate arrangement was randomized before each run. For increased efficiency, the new reaction rate is obtained by running only for a short time (10^{-9} – 10^{-5} s in the absence of lateral interactions; 10^{-10} – 1 s in the presence of lateral interactions) using a new reaction constant.

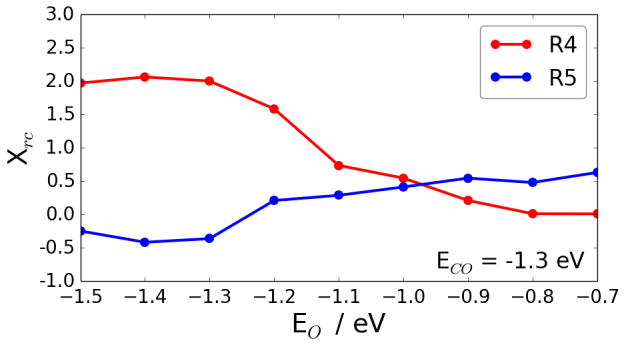

Figure 4: Degree of rate control (X_{rc}) for significant reaction steps R4 and R5 during CO oxidation in the absence of lateral interactions from kMC simulations at $T = 600\,K$, $P_{O_2} = 0.33\,bar$, $P_{CO_2} = 1.0\,bar$, $P_{co} = 0.67\,bar$. The X_{rc} values were calculated along the dashed white line in Figure 1 (b,d) corresponding to E_{CO} = -1.3 eV.

Despite the described efforts to increase computational efficiency and reduce noise, the repeated evaluation of finite differences for each reaction step using the kMC model remains costly and the noise was not fully eliminated. Hence, the equivalent 2D representation of X_{rc} as shown in Figure 2 for MKM is difficult to analyze. Instead, we performed the X_{rc} analysis along a one-dimensional cut parallel to E_O that passes through the top of the volcano at a constant $E_{CO} = -1.3\ eV$, as indicated by the dashed white line in Figure 1**Error! Reference source not found.**(b, d). The outcome is presented in Figure 4. In agreement with the MKM results, the degree of rate control value for R3 is essentially zero for the entire range of O* binding energies, indicating that these steps are not rate-limiting and therefore omitted in Figure 4. Moreover, the lack of sensitivity to the rate constants of steps R1 and R2 in the kMC model validates the quasi-equilibrium assumptions made for the MKM. As shown in Figure 4, in the region where E_O is lower than -1.0 eV, which is also the region where the surface is fully covered by O* (Figure 1d), R4 is rate-limiting with $X_{rc,R4} \approx 2$. The rate-determining step shifts to R5 at the top of the volcano as E_O becomes weaker.

As expected, in the absence of lateral adsorbate-adsorbate interactions the MKM and kMC simulations predict identical reactivity and coverage trends and yield fully consistent mechanistic information, despite minor differences in the absolute TOF. Considering the higher computational cost and more difficult degree of rate control analysis, we may conclude at this point that if no adsorbate-adsorbate interactions are included and the spatial arrangement of active sites is uniform, the MKM approach is clearly preferable.

3.2 Reactivity trends in the presence of lateral interactions

Lateral interactions among co-adsorbed intermediates are known to play an important role in catalysis by modifying the activation energies and reaction energies of elementary processes [33,34]. Lateral interactions may also lead to the formation of ordered adlayers for which the mean-field approximation breaks down. To assess the consequences of including lateral interactions into descriptor-based trend studies using MKM and kMC solvers, we rerun the kinetic trends models with two sets of interaction energy (IE) parameters. The first set was adopted from Grabow *et al.* for Pt(111) and contains only repulsive nearest neighbor interaction terms [13]. The pairwise energy contribution are 0.242 eV for O*-O*, 0.232 eV for CO*-CO*, and 0.102 eV for CO*-O* interactions. For the second set of parameters that also includes attractive second nearest neighbor interactions we adopted the DFT values reported by Nagasaka *et al*. on Pt(111) [34]. Both interaction parameter sets are summarized in Table 1.

Table 1: Lateral Interaction Energy (IE) Parameters

Co-adsorbed Species	IE (eV)	
	Set 1 (Grabow *et al.* [13])	Set 2 (Nagasaka *et al.* [34])
O*-O*	0.242	0.238
CO*-CO*	0.232	0.263
CO*-O*	0.102	0.009
O*-*-O* (120°)	-	-0.006
O*-*-O* (180°)	-	-0.027
CO*-*-CO* (120°)	-	-0.008

With purely repulsive lateral interactions for O*-O*, CO*-CO*, and CO*-O* from Set 1 implemented within the mean-field approximation, the MKM simulation in Figure 5(a) produces a rate map with a broad plateau and a peak position that is noticeably shifted to more negative descriptor values. The origin for the excessively broad peak is discussed in Grabow *et al.* [13] and can be attributed to the use of the differential binding energy of O* and CO* at high coverage as descriptors. The strongly binding metals reach a saturation coverage of O* or CO* below 1 ML, implying that vacant sites remain available even for metals with strongly negative binding energies at zero coverage. Moreover, metals with a high affinity for oxygen are prone to oxidation, which is a limitation we have not accounted for. A closer inspection using specific interaction parameters for each metal and considering oxide formation showed that the volcano peak undergoes only a mild shift to more negative descriptor values when repulsive interactions are included.[13] Thus, the elongated shape of the broad plateau and the indicated peak at (-2.5, -2.5) in Figure 5(a) are an artifact of the coverage treatment and should not be overinterpreted. A more realistic target would be the top right tip of the elliptic rate tableau near (-1.4, -1.6). The artificially elongated elliptical shape of the activity plateau may also lead to the incorrect conclusion that $E_O \approx E_{CO}$ always results in an active catalyst. For CO oxidation, an optimal catalyst has approximately equal coverages of O*, CO* and empty sites, but since the mean-field implementation of the coverage dependence directly on the activity descriptors avoids surface poisoning even for strongly binding metals, the disappearance of vacant sites is insufficiently captured. In further agreement with Grabow *et al.* we find that the maximum TOF with and without interactions retains the same order of magnitude at the top of the volcano, the low coverage region in the top right corner of the descriptor space does not change, and the order of catalytic activity between metal candidates is consistent with Figure 1(a), obtained in the absence of interactions.[13]

In contrast, the kMC model explicitly treats pairwise additive lateral interactions between the nearest neighbors included in Set 1 (O*-O*, CO*-CO*, CO*-O*). This different interaction treatment leads to pronounced differences between the MKM solution in Figure 5(a) and the kMC solution in Figure 5(c). For instance, the peak of the volcano obtained from kMC remains well-defined and rapidly drops when the descriptor values become too negative. The peak remains closer to the position obtained without any interaction (Figure 1c). Without emphasizing the agreement of the kMC peak location at (-1.5, -1.7) and the top of the elliptic rate tableau at (-1.4, -1.6) from MKM, we want to focus on the qualitative agreement that the peak moves to more negative descriptor values in both approaches when repulsive interactions are included, such that Pt and Pd are now too weakly binding. The maximum TOF from the kMC simulation is two orders of magnitude higher than the maximum TOF from MKM. We are again able to eliminate surface diffusion as a possible origin of the differences, which we verified by varying the rate constants for the surface diffusion steps in the kMC model. As shown in the event frequency graph in Figure S2, all diffusion steps are quasi-equilibrated and rapid surface rearrangement is kinetically feasible.

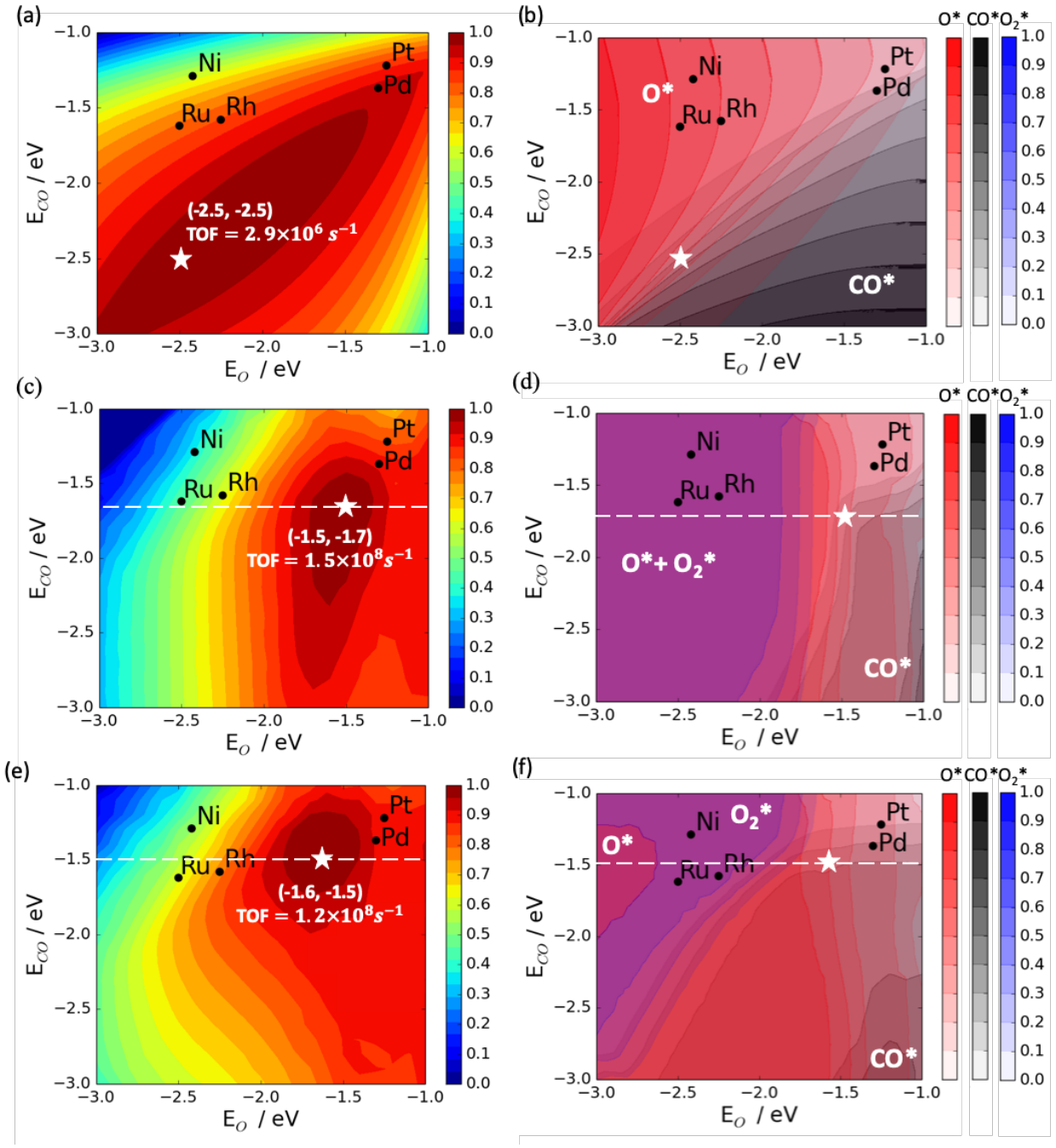

Figure 5: Comparison of trend predictions for CO oxidation as a function of E_O and E_{CO} from MKM (a, b), kMC with interaction energies from Set 1 (c, d) and kMC with interaction energies from Set 2 (e, f) at $T = 600\ K$, $P_{O_2} = 0.33\ bar$, $P_{CO_2} = 1.0\ bar$, $P_{co} = 0.67\ bar$. The normalized TOF is shown in contour plots obtained from (a) MKM and (c, e) kMC. The corresponding surface coverages of O* (red), CO* (black), and O_2* (blue) are provided in panels (b) for MKM and (d, f) for kMC. The coverage of O_2* is always $< 2 \times 10^{-5}$ ML in the MKM approach and is not included in panel (b). The star marks the point of maximum activity and the corresponding coordinates in descriptor space are provided in parentheses. The color depth in (b, d, f) is linearly correlated with

the coverage. The horizontal dashed line in panels (c, d) and (e, f) represents a fixed value of $E_{CO} = -1.7\ eV$ and $E_{CO} = -1.5\ eV$, respectively, used in the degree of rate control analyses for the kMC model.

Marked differences between MKM and kMC results are also found for surfaces coverages shown in Figure 5(b, d). An accompanying snapshot of the kMC lattice configuration at the point of highest activity is provided in Figure S3. The commonality of the MKM and kMC results is that the point of maximum activity is found at the border of O* and CO* covered regions. Thus, we can infer that the observed activity trend differences can be attributed to different surface coverages resulting from the different treatment of lateral interactions. Notably, we observe a large region in Figure 5(d) where a mixed O*/O_2* surface phase is stable and the low concentration of CO* limits O*/O_2* removal. Considering the very low O_2* coverages we obtained in the absence of interactions as well as in the MKM solution with repulsive interactions, the high coverage of O_2* is somewhat unexpected. The emergence of the extended O*/O_2* phase can be explained, however, as difference in the propagation behavior of the coverage dependence in the MKM and kMC approach. As described in the SI, the iterative solution of the coverage dependent MKM makes adjustments to the descriptor values, which in turn alters the binding energy of O_2* at high coverages through the scaling relation in Eq. (6). The kMC approach requires explicit IEs between all adsorbates; thus, the missing O_2*-O_2* and O_2*-O* interactions allow O* and O_2* to pack densely without energy penalty. Significant amounts of surface CO* only form for weaker values of E_O, which explains why the volcano peak remains closer to the Pd and Pt points. While the kMC approach is powerful and has the potential to capture adsorbate-adsorbate interactions more accurately than the mean-field MKM approach, this example illustrates that a complete set of interaction parameters is required to correctly predict spatially-resolved active site occupancies in a 2D lattice. Omitting certain interactions can have unintended consequences. In the mean-field description of the MKM approach the globally high coverage of O* reduces the stability and coverage of O* and O_2* via Eq. (6), allowing CO* to show up even for strongly negative values of E_O. Hence, the mean-field implementation is generally more forgiving. In an attempt to close the gap between the MKM and kMC solution, we have estimated repulsive O_2*-O_2* and O_2*-O* IE parameters from the scaling relations as detailed in the SI. If such an estimation was to be avoided, these additional IE parameters would need to be calculated from DFT. Moreover, each additional model parameter increases the model complexity, whereas computational catalyst screening builds on the premise of complexity reduction. After explicitly including interactions for O_2*, our results in Fig. S4 show as expected that the O*/O_2* phase disappears and the O_2* coverage is negligible throughout the descriptor space. The rate maximum is shifted to (-1.8, -1.6), i.e., mildly stronger O* binding, and a second maximum emerges in a dominantly CO* covered region at the upper limit of E_O at (-1.0, -2.0). A closer inspection of Figure 5(c) suggests that this second maximum already existed before the IE parameters for O_2* were introduced, but it was simply cut off. No second maximum could be observed in the MKM implementation.[13] The two maxima in the kMC approach correspond to two different sets of optimal combinations of rate constants and surface coverages, where the first peak has a higher O* coverage and the second peak has a higher CO* coverage. We also note that the saddle point between both peaks has approximately equal O* and CO* coverage with empty sites available, but despite the more favorable surface coverage, the rate constants for the rate determining steps R4 and R5 are lower. This unexpected result can be rationalized by inspection of the interaction parameters in Table 1. The repulsive interactions between identical species CO*-CO* and O*-O* are more than twice as

strong as those for the mixed CO*-O* interaction. Hence, at approximately equal total coverage, the mixed CO*-O* overlayer at the saddle point is more stable than either the O*-rich or CO*-rich overlayer at the two peaks. The higher stability of the mixed CO*-O* adlayer favors the initial state of step R4 such that the coverage corrections to the activation energy barrier result in a lower effective rate constant compared to that for the less stable O*- and CO*-rich overlayers. The analogous argument can be made for step R5 because we based our interaction energy estimate for O_2*-O_2* and O_2*-O* repulsion on that of O*-O*. This example effectively illustrates the ability of kMC to capture complex coverage and reactivity scenarios, but it also demonstrates the sensitivity of kMC predictions to the parameter choice.

For the MKM model with lateral interactions we continue to observe two coverage regions in Figure 5(b), i.e., the O* and CO* covered region. As already discussed for Figure 2, the change of most abundant surface intermediate coincides with a change in the rate control of steps R4 and R5; Figure 6(a) shows that the degree of rate control values for R4 increase from the strong CO* binding region to the strong O* binding region from the bottom right to the top left, which indicates that the removal of O* by oxidation with CO* is a single rate-determining step in the strong O* binding region. Conversely, the degree of rate control values for R5 increase from the strong O* binding region to the strong CO* binding region from the top left to the bottom right, implying that the CO*-assisted dissociation of O_2* becomes a partially rate-determining step in the strong CO* binding region. A comparison between Figure 2 and Figure 6 shows consistent degree of rate control values in the CO*-covered region, while the sensitivity in the O*-covered region is lessened. This can be explained by the lower O* coverage and availability of empty sites which effectively decouples R4 and R5; with empty sites always available the adsorption of CO* and O_2* does not depend on the creation of two empty sites after R4. Consistent with the results in the absence of lateral interactions, the direct dissociation of O_2*, R3, does not have any significant contributions to O_2* activation; thus, its degree of rate control is practically zero.

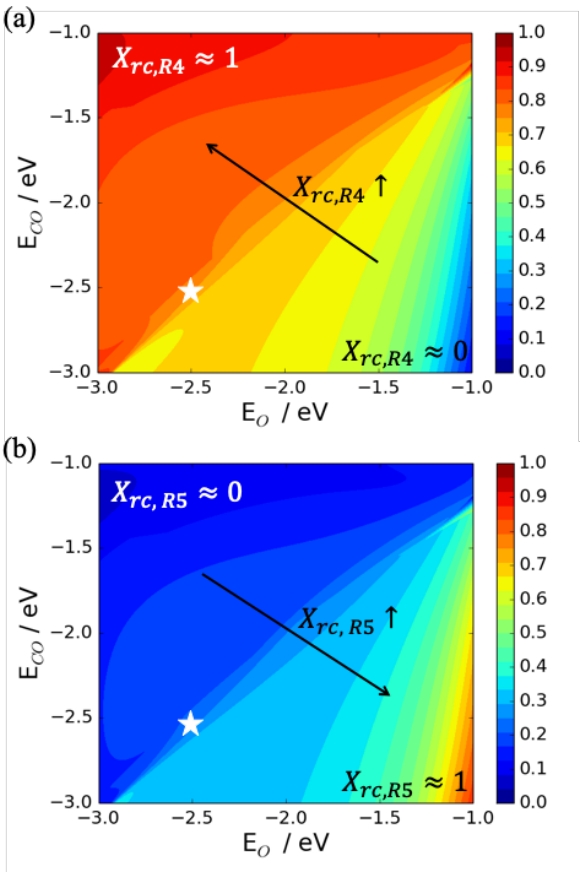

Figure 6: Degree of rate control (X_{rc}) for significant reaction steps (a) R4 and (b) R5 during CO oxidation in the presence of repulsive interactions between O*-O*, CO*-CO*, and CO*-O* from the MKM model at $T = 600\ K$, $P_{O_2} = 0.33\ bar$, $P_{CO_2} = 1.0\ bar$, $P_{co} = 0.67\ bar$. The star marks the point of maximum activity.

To examine the degree of rate control predicted by the kMC approach with repulsive interaction parameters, we limit ourselves again to an analysis along the horizontal line in Figure 5(c, d), defined by a constant value of $E_{CO} = -1.7$ eV, which includes an intersection with the TOF maximum. Consistent with all other cases, the degree of rate control for R1, R2, and R3 is always near zero and not further discussed. Figure 7 shows that the degree of rate control for step R5 increases at the expense of R4 as the affinity of the catalysts to oxygen decreases. This observation is by and large consistent with the MKM results presented in Figure 6, but in the kMC case, the shift of the rate-determining step coincides with the peak of the volcano at $E_O = -1.5$ eV.

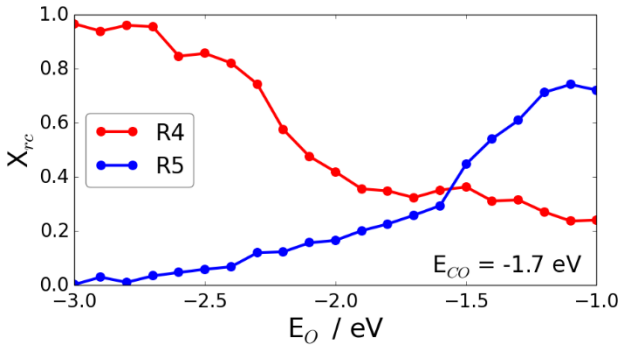

Figure 7: Degree of rate control (X_{rc}) for reaction steps R4 and R5 during CO oxidation in the presence of repulsive interactions between O*-O*, CO*-CO*, and CO*-O* from kMC simulations at $T = 600\ K$, $P_{O_2} = 0.33\ bar$, $P_{CO_2} = 1.0\ bar$, $P_{co} = 0.67\ bar$. The X_{rc} values were calculated along the dashed white line in Figure 5(c,d) corresponding to E_{CO} = -1.7 eV.

Thus far, we only discussed repulsive interactions, which alter the stabilities of surface intermediates and transitions states leading to differences in coverage and rates depending on the implementation. Repulsive forces can theoretically also result in non-ideal, segregated surface coverages; for instance, if A-B repulsion was large, but A-A and B-B interactions are small, the surface would be populated by islands of pure A and pure B, but not a well-mixed A-B adlayer. We are not aware of such a scenario with practical relevance and instead consider the attractive second nearest neighbor interactions between O* on Pt(111). Attractive interactions are the most typical reason for the formation of adsorbate islands, with the implication that bimolecular reactions may only occur at the boundary of two adjacent surface phases. Here we adopt the DFT values calculated by Nagasaka *et al.* [34] on Pt(111) for the attractive interactions between the second nearest-neighbor O*-*-O* clusters, where the angles between O*-* and *-O* are 180° and 120°, respectively, and the repulsive second nearest-neighbor CO*-*-CO*, where the angle between CO*-* and *-CO* is 120°. Their interaction parameters for the nearest neighbor interaction between O*-O*, CO*-CO*, and CO*-O* are in good agreement with the exclusively repulsive set by Grabow *et al.* as the direct comparison in Table 1 shows.

We modified our kMC model with the repulsive and attractive interaction parameters from Set 2 in Table 1 and obtained the results displayed in Figure 5(e, f). The activity plot in Figure 5(e) shows strong resemblance to Figure 5(b), which is not surprising given the nearly identical repulsive interactions in Sets 1 and 2, and the rather small attractive interaction energies in Set 2. Figure S5 also shows a fairly random ordering of the mixed adsorbate layer for the peak position in Figure 5(e). The degree of rate control analysis along the horizontal line in Figure 5(e, f) defined by a constant value of $E_{CO} = -1.5$ eV is consistent with all other cases. The peak of the volcano at $E_O = -1.6$ eV is the point where the rate-determining step shifts from R4 to R5. The remaining reactions are quasi-equilibrated.

Nevertheless, the small attractive interactions between the second nearest-neighbor O*-*-O* clusters are strong enough to stabilize O*, which is reflected as higher O* and lower O_2* coverage for surfaces with high oxygen affinity shown in Figure 5(f). Yet, the weak attractive interactions are not strong enough to form pronounced islands within the descriptor space we considered. Figure S6 obtained for an O*-rich surface only shows evidence for the formation of O*-*-O* motives with the stabilized 180° and 120° angles. Our finding is in agreement with

Piccinin *et al*. [35], who reported a similar kMC study of CO oxidation on Pd(111) and were also unable to observe extended O* islands.

3.3 Trend comparison between MKM and kMC

The value of descriptor-based screening studies lies in the ability to rank order catalysts depending on their activity or selectivity and to extract mechanistic trend information across the periodic table [36]. This information is to be obtained using the smallest possible number of reactivity descriptors. The majority of trend studies relies on 1-2 descriptors and considering the many approximations in this approach it is certainly unrealistic to expect reliable absolute reaction rates or coverages. Near the volcano peak and in areas with steep slopes the placement of metals onto the activity map is also associated with large uncertainties and we noted at strong sensitivity of kMC predictions on the choice of interaction parameters. In Table 2 we have compiled a ranking of monometallic catalysts according to their predicted TOF for CO oxidation as obtained from MKM or kMC methods, with and without lateral interactions. Despite the large differences we have noted for absolute TOFs and surface coverages, we find that the relative rank ordering is nearly invariable in all cases. Besides, the same rate-determining steps were consistently identified using a degree of rate control analysis. Only when we estimated IEs for O_2*-O_2* and O_2*-O* interactions used in the kMC model, we found a higher activity for Rh and lower activity for Pt; however, this ordering could be easily reversed if the E_{CO} descriptor for Pt was 0.2 eV more negative and 0.2 eV more positive for Rh. A deviation of 0.2 eV would be considered a common error bar in the placement of metals in the descriptor domain.

Table 2: The Rank Order of Metals from kMC and MKM approaches in the Absence and Presence of Lateral Interaction Energies (IEs).

From kMC				From MKM	
No interactions	IE Set 1	IE Set 1 + O_2*[a]	IE Set 2	No interactions	IE Set 1
Pd	Pd	Rh	Pd	Pd	Pd
Pt	Pt	Pd	Pt	Pt	Pt
Rh	Rh	Ru	Rh	Rh	Rh
Ru	Ru	Pt	Ru	Ru	Ru
Ni	Ni	Ni	Ni	Ni	Ni

[a] The pairwise IE parameters for O_2*-O_2* and O_2*-O* were estimated from scaling relationships as detailed in the SI.

For the particular example of CO oxidation at elevated temperature, we find that using a MKM even in the presence of adsorbate-adsorbate interactions is accurate enough to study activity trends. Considering its easier implementation and high computational efficiency, a MKM is preferred over the more sophisticated and expensive kMC approach. We emphasize, however, that this should not be misunderstood as a general recommendation; the mean-field assumption has limitations and can indeed break down for cases with high surface heterogeneity, such as the surface island formation due to strong lateral adsorbate-adsorbate interactions or catalysts with multiple spatially distributed active sites, possibly coupled with slow surface diffusion. Depending on the implementation of coverage effects, the mean-field approach is also likely to overpredict

the activity of highly reactive metals. If these phenomena are known to exist, then the additional cost of a kMC simulation is justified to produce more differentiated outcomes.

4. Conclusions

We have performed a cost-benefit analysis for using mean-field MKM versus lattice kMC approaches as kinetic models in the context of descriptor-based catalyst screening. The analysis was performed for the CO oxidation reaction at elevated temperature with and without lateral adsorbate interactions as test case. In the absence of coverage effects and random adsorbate distributions on the surface, the MKM approach is superior. When lateral interactions are included, however, the outputs from MKM and kMC simulations show large differences in terms of absolute reaction rates and surface coverages. The possibility of slow diffusion in the kMC approach was eliminated, such that all differences can be attributed to the description of lateral interactions using the mean-field approximation in MKM and the cluster expansion in kMC.

The detailed spatial resolution of site and adsorbate distributions offered by kMC along with the possibility to capture local environment effects with a cluster expansion constitutes a big advantage. But this benefit comes at the price of a three orders of magnitude increased computational cost and the need for a long list of interaction parameters, which also add a significant cost when obtained from first principles calculations. Another challenge when using the kMC approach is its high sensitivity toward the included interaction parameters. The higher computational expense can be justified if surface heterogeneities are known to be important for a particular system, but for exploratory catalyst design studies the information of interest is often limited to a relative rank ordering of materials and mechanistic trends. Assuming a computational screening scenario with a minimal set of available activity descriptors, MKM, even without considering lateral interactions, provides sufficiently accurate information regarding the rank ordering and activity trends. A degree of rate control analysis consistently showed that CO oxidation with O* (R4) is rate-determining at high O* coverage, whereas CO oxidation with O_2* is rate-determining in CO* covered regions, regardless of using MKM or kMC implementations. Unless, there is a justified need for the spatial resolution afforded by kMC simulations, our analysis suggests that MKM offers the best compromise between affordable computational cost and meaningful catalytic trend predictions.

Acknowledgments

This work has been funded by the U.S. Department of Energy (DOE), Office of Science, Office of Basic Energy Sciences under award number DE-SC0011983. This research used resources of the National Energy Research Scientific Computing Center (NERSC), a U.S. Department of Energy Office of Science User Facility operated under Contract No. DE-AC02-05CH11231. The authors acknowledge the use of the Maxwell/Opuntia/Sabine Cluster and the advanced support from the Research Computing Data Core at the University of Houston to carry out the research presented here.

References:

[1] J.A. Dumesic, D.F. Rudd, L.L. Aparicio, J.E. Rekoske, A.A. Treviño, The Microkinetics of Heterogeneous Catalysis, American Chemical Society, Washington, DC, 1993.

[2] J.A. Dumesic, G.W. Huber, M. Boudart, Rates of Catalytic Reactions, in: G. Ertl, H. Knözinger, F. Schüth, J. Weitkamp (Eds.), Handb. Heterog. Catal., 2nd ed., Wiley-VCH

Verlag GmbH & Co. KGaA, 2008.
[3] H.J. Li, A.C. Lausche, A.A. Peterson, H.A. Hansen, F. Studt, T. Bligaard, Using microkinetic analysis to search for novel anhydrous formaldehyde production catalysts, Surf. Sci. 641 (2015) 105–111. https://doi.org/10.1016/j.susc.2015.04.028.
[4] A.J. Medford, C. Shi, M.J. Hoffmann, A.C. Lausche, S.R. Fitzgibbon, T. Bligaard, J.K. Nørskov, CatMAP: A Software Package for Descriptor-Based Microkinetic Mapping of Catalytic Trends, Catal. Letters. 145 (2015) 794–807. https://doi.org/10.1007/s10562-015-1495-6.
[5] T. Bligaard, J.K. Nørskov, S. Dahl, J. Matthiesen, C.H. Christensen, J. Sehested, The Br{ø}nsted-Evans-Polanyi relation and the volcano curve in heterogeneous catalysis, J. Catal. 224 (2004) 206–217.
[6] L.C. Grabow, Computational Catalyst Screening, in: A. Asthagiri, M.J. Janik (Eds.), Comput. Catal., Royal Society of Chemistry, Cambridge, UK, 2014: pp. 1–58.
[7] M.M. Montemore, J.W. Medlin, Scaling relations between adsorption energies for computational screening and design of catalysts, Catal. Sci. Technol. 4 (2014) 3748–3761. https://doi.org/10.1039/C4CY00335G.
[8] D.A. Hansgen, D.G. Vlachos, J.G. Chen, Using first principles to predict bimetallic catalysts for the ammonia decomposition reaction, Nat. Chem. 2 (2010) 484–489. https://doi.org/10.1038/nchem.626.
[9] L.T. Roling, F. Abild-Pedersen, Structure-Sensitive Scaling Relations: Adsorption Energies from Surface Site Stability, ChemCatChem. 10 (2018) 1643–1650. https://doi.org/10.1002/cctc.201701841.
[10] G. Kumar, E. Nikolla, S. Linic, J.W. Medlin, M.J. Janik, Multicomponent Catalysts: Limitations and Prospects, ACS Catal. (2018) 3202–3208. https://doi.org/10.1021/acscatal.8b00145.
[11] J. Saavedra, H.A. Doan, C.J. Pursell, L.C. Grabow, B.D. Chandler, The critical role of water at the gold-titania interface in catalytic CO oxidation, Science (80-.). 345 (2014) 1599–1602. https://doi.org/10.1126/science.1256018.
[12] T.O. Omotoso, B. Baek, L.C. Grabow, S.P. Crossley, Experimental and First-Principles Evidence for Interfacial Activity of Ru/TiO 2 for the Direct Conversion of m -Cresol to Toluene, ChemCatChem. 9 (2017) 2642–2651. https://doi.org/10.1002/cctc.201700157.
[13] L.C. Grabow, B. Hvolbæk, J.K. Nørskov, Understanding Trends in Catalytic Activity: The Effect of Adsorbate–Adsorbate Interactions for CO Oxidation Over Transition Metals, Top. Catal. 53 (2010) 298–310. https://doi.org/10.1007/s11244-010-9455-2.
[14] J. Lu, A. Heyden, Theoretical investigation of the reaction mechanism of the hydrodeoxygenation of guaiacol over a Ru(0001) model surface, J. Catal. 321 (2015) 39–50. https://doi.org/10.1016/j.jcat.2014.11.003.
[15] J.E. De Vrieze, J.W. Thybaut, M. Saeys, Role of Surface Hydroxyl Species in Copper-Catalyzed Hydrogenation of Ketones, ACS Catal. 8 (2018) 7539–7548. https://doi.org/10.1021/acscatal.8b01652.
[16] K. Reuter, M. Scheffler, First-principles kinetic Monte Carlo simulations for heterogeneous catalysis: Application to the CO oxidation at RuO2(110), Phys. Rev. B. 73 (2006) 045433. https://doi.org/10.1103/PhysRevB.73.045433.
[17] A. Chatterjee, D.G. Vlachos, An overview of spatial microscopic and accelerated kinetic Monte Carlo methods, J. Comput. Mater. Des. 14 (2007) 253–308. https://doi.org/10.1007/s10820-006-9042-9.

[18] M. Stamatakis, Kinetic modelling of heterogeneous catalytic systems, J. Phys. Condens. Matter. 27 (2015) 013001. https://doi.org/10.1088/0953-8984/27/1/013001.
[19] J.M. Sanchez, F. Ducastelle, D. Gratias, Generalized cluster description of multicomponent systems, Phys. A Stat. Theor. Phys. 128 (1984) 334–350.
[20] M.J. Hoffmann, T. Bligaard, A Lattice Kinetic Monte Carlo Solver for First-Principles Microkinetic Trend Studies, J. Chem. Theory Comput. 14 (2018) 1583–1593. https://doi.org/10.1021/acs.jctc.7b00683.
[21] H. Falsig, B. Hvolbæk, I.S. Kristensen, T. Jiang, T. Bligaard, C.H. Christensen, J.K. Nørskov, Trends in the catalytic CO oxidation activity of nanoparticles, Angew. Chemie-International Ed. 47 (2008) 4835–4839.
[22] R.D. Cortright, J.A. Dumesic, Kinetics of heterogeneous catalytic reactions: Analysis of reaction schemes, Adv. Catal. 46 (2001) 161. https://doi.org/10.1016/S0360-0564(02)46023-3.
[23] G.N. Lewis, D.F. Smith, The theory of the reaction rate, J. Am. Chem. Soc. 47 (1925) 1508–1520. https://doi.org/10.1021/ja01683a004.
[24] A.U. Nilekar, J. Greeley, M. Mavrikakis, A simple rule of thumb for diffusion on transition-metal surfaces., Angew. Chem. Int. Ed. Engl. 45 (2006) 7046–9. https://doi.org/10.1002/anie.200602223.
[25] M. Stamatakis, D.G. Vlachos, A graph-theoretical kinetic Monte Carlo framework for on-lattice chemical kinetics., J. Chem. Phys. 134 (2011) 214115. https://doi.org/10.1063/1.3596751.
[26] J. Nielsen, M. D'Avezac, J. Hetherington, M. Stamatakis, Parallel kinetic Monte Carlo simulation framework incorporating accurate models of adsorbate lateral interactions, J. Chem. Phys. 139 (2013) 224706. https://doi.org/10.1063/1.4840395.
[27] M. Stamatakis, D.G. Vlachos, Equivalence of on-lattice stochastic chemical kinetics with the well-mixed chemical master equation in the limit of fast diffusion, Comput. Chem. Eng. 35 (2011) 2602–2610. https://doi.org/10.1016/j.compchemeng.2011.05.008.
[28] B. Temel, H. Meskine, K. Reuter, M. Scheffler, H. Metiu, Does phenomenological kinetics provide an adequate description of heterogeneous catalytic reactions?, J. Chem. Phys. 126 (2007) 204711–204712.
[29] M. Andersen, C.P. Plaisance, K. Reuter, Assessment of mean-field microkinetic models for CO methanation on stepped metal surfaces using accelerated kinetic Monte Carlo, J. Chem. Phys. 147 (2017) 152705. https://doi.org/10.1063/1.4989511.
[30] C.T. Campbell, Future Directions and Industrial Perspectives Micro- and macro-kinetics: Their relationship in heterogeneous catalysis, Top. Catal. 1 (1994) 353–366.
[31] C.T. Campbell, The Degree of Rate Control: A Powerful Tool for Catalysis Research, ACS Catal. 7 (2017). https://doi.org/10.1021/acscatal.7b00115.
[32] F. Hess, H. Over, Rate-Determining Step or Rate-Determining Configuration? The Deacon Reaction over RuO 2 (110) Studied by DFT-Based KMC Simulations, ACS Catal. 7 (2017) 128–138. https://doi.org/10.1021/acscatal.6b02575.
[33] D. Mei, P.A. Sheth, M. Neurock, C.M. Smith, First-principles-based kinetic Monte Carlo simulation of the selective hydrogenation of acetylene over Pd(111), J. Catal. 242 (2006) 1–15. https://doi.org/10.1016/j.jcat.2006.05.009.
[34] M. Nagasaka, H. Kondoh, I. Nakai, T. Ohta, CO oxidation reaction on Pt(111) studied by the dynamic Monte Carlo method including lateral interactions of adsorbates, J. Chem. Phys. 126 (2007) 44704–44707.

[35] S. Piccinin, M. Stamatakis, CO oxidation on Pd(111): A first-principles-based kinetic monte carlo study, ACS Catal. 4 (2014) 2143–2152. https://doi.org/10.1021/cs500377j.
[36] B. Baek, A. Aboiralor, S. Wang, P. Kharidehal, L.C. Grabow, J.D. Massa, Strategy to improve catalytic trend predictions for methane oxidation and reforming, AIChE J. 63 (2017) 66–77. https://doi.org/10.1002/aic.15404.
[37] L.C. Grabow, A.A. Gokhale, S.T. Evans, J.A. Dumesic, M. Mavrikakis, Mechanism of the water gas shift reaction on Pt: First principles, experiments, and microkinetic modeling, J. Phys. Chem. C. 112 (2008) 4608–4617.

Supplementary Information for

"Evaluating the Benefits of Kinetic Monte Carlo and Microkinetic Modeling for Catalyst Design Studies in the Presence of Lateral Interactions"

*Xiao Li and Lars C. Grabow**

William A. Brookshire Department of Chemical and Biomolecular Engineering, University of Houston, Houston, TX 77204-4004, USA

*grabow@uh.edu

Table of Contents

Iterative solution of the coverage-dependent microkinetic model

The solution of the coverage-dependent microkinetic model (MKM) was obtained with the iterative procedure described in Ref [13]. Using the predicted surface coverage from an analytical solution to the coverage independent model at each descriptor value pair (E_O, E_{CO}), the differential coverage-corrected binding energy for O* and CO* was calculated according to

$$E_O^{diff}(\theta_O, \theta_{CO}) = E_O^0 + \underbrace{2\varepsilon_{O-O}(\theta_O - \theta_O^0)}_{if\ \theta_O - \theta_O^0 > 0} + \underbrace{\varepsilon_{0,O-CO}\theta_{CO}^* + \frac{3}{2}\varepsilon_{1,O-CO}\theta_{CO}^*\sqrt{\theta_O^*\theta_{CO}^*}}_{if\ \theta_O^* > 0\ and\ \theta_{CO}^* > 0}$$

$$E_{CO}^{diff}(\theta_O, \theta_{CO}) = E_{CO}^0 + \underbrace{2\varepsilon_{CO-CO}(\theta_{CO} - \theta_{CO}^0)}_{if\ \theta_{CO} - \theta_{CO}^0 > 0} + \underbrace{\varepsilon_{0,O-CO}\theta_O^* + \frac{3}{2}\varepsilon_{1,O-CO}\theta_O^*\sqrt{\theta_O^*\theta_{CO}^*}}_{if\ \theta_O^* > 0\ and\ \theta_{CO}^* > 0}$$

where all symbols carry the same meaning as in Ref [13]; E_x^0 is the zero-coverage binding energy of species x, θ_x is the coverage of species x, θ_x^0 denotes a threshold coverage below which lateral interaction are neglected, θ_x^* is an effective coverage as defined in Ref [13], and ε values indicate interaction energies. Here, we used the reported model parameters for Pt(111), which are tabulated in Table S1.

Table S3: Interaction model parameters according to Ref [13]

θ_O^0	0.18 ML	θ_{CO}^0	0.24 ML
ε_{O-O}	1.45 eV/ML	ε_{CO-CO}	1.39 eV/ML
$\varepsilon_{0,O-CO}$	0.61 eV/ML	$\varepsilon_{1,O-CO}$	3.57 eV/ML^2

The values $\left(E_O^{diff}, E_{CO}^{diff}\right)$ were then used as the updated descriptors for the binding energy of O* and CO* and are subsequently used in the scaling relations Eq. (3) – (7). We note that by applying the coverage correction to the descriptor values all other energies including the binding energy of O_2* and all transition state energies are also affected.

Using the coverage-corrected descriptor pair, the microkinetic model is solved again for new steady-state coverages, resulting in a new set of descriptor values. This loop is repeated until the coverages and descriptor values no longer change.

Coverage dependency in the kinetic Monte Carlo model

For a comparable treatment of adsorbate-adsorbate interactions in the kMC simulation, we made the following adjustments from the MKM implementation. The 2nd order interaction model for *O-CO* interactions was simplified to 1st order as necessitated by counting only first nearest neighbor interactions in the kMC model.

$$\varepsilon_{O-CO} = \varepsilon_{0,O-CO} + \varepsilon_{1,O-CO}\sqrt{\theta_O^*\theta_{CO}^*} \approx \varepsilon_{0,O-CO} = 0.61\,\frac{eV}{ML}$$

The interaction parameters $\varepsilon_{O-O} = 1.45\,\frac{eV}{ML}$, $\varepsilon_{CO-CO} = 1.39\,\frac{eV}{ML}$, and $\varepsilon_{O-CO} = 0.61\,\frac{eV}{ML}$.

were then divided by 6, because there are 6 nearest neighbors in a complete ML. The resulting values describe pairwise interactions between surface species. A cluster expansion is used for the calculation of the energy of the lattice for a given configuration[35]:

$$H(\sigma) = \sum_{k=1}^{N_C} \frac{ECI_k}{GM_k} \cdot NCE_k(\sigma)$$

where $H(\sigma)$ denotes the Hamiltonian of the system (energy of a configuration); N_C is the number of clusters specified in the energetic model; ECI_k is the effective cluster interaction of figure k, namely, the contribution of one such figure to the total energy; GM_k is the graph-multiplicity of that figure; and NCE_k is the number of occurrences of figure k in the current lattice configuration, obtained by performing a pattern search on the lattice and counting the possible mappings of figure k on the adlayer.

The reaction energy is

$$\Delta E_{rxn}(\sigma) = H(\sigma') - H(\sigma) + \Delta E_{gas}$$

where σ' and σ are the final and initial lattice configurations; ΔE_{gas} is the difference in the gas species energies between final and initial configurations; H is the Hamiltonian.

The lateral interaction parameters propagate to the activation energy barriers based on the energies of lattice configurations

$$E_{fwd}^{\ddagger} = max\left(0, \Delta E_{rxn}(\sigma), E_{fwd,0}^{\ddagger} + \omega \cdot \left(\Delta E_{rxn}(\sigma) - \Delta E_{rxn,0}\right)\right)$$

$$E_{rev}^{\ddagger} = max\left(-\Delta E_{rxn}(\sigma), 0, E_{rev,0}^{\ddagger} - (1-\omega) \cdot \left(\Delta E_{rxn}(\sigma) - \Delta E_{rxn,0}\right)\right)$$

where $E_{fwd,0}^{\ddagger}$ and $E_{rev,0}^{\ddagger}$ are the activation energies of the forward and reverse step at the zero-coverage limit; ω is a parameter termed the proximity factor[37]; and $\Delta E_{rxn,0}$ is the reaction energy at the zero-coverage limit.

The explicit treatment of nearest neighbor interactions between O* and CO*, however, does not have any effect on the binding energy of O_2*. This is in stark contrast to the MKM approach, where the coverage-adjusted descriptor for O* propagated the repulsive interactions to O_2*. We attempted to correct this and approximated the interaction energy between O_2* and O* and the interaction energy between O_2* and O_2* based on scaling relations. From Eq. (6) we applied the scaling factor of 0.8928 to the O*-O* interaction energy from Set 1 and obtained $IE_{O_2*-O_2*} = 0.8928 \times IE_{O*-O*} = 0.216\ eV$. The O_2*-O* interaction energy taken as the average of the O_2*-O_2* interaction energy and the O*-O* interaction energy, $IE_{O_2*-O*} = \frac{1}{2}\left(IE_{O_2*-O_2*} + IE_{O*-O*}\right) = \frac{1}{2}(0.216 + 0.242) = 0.229\ eV$.

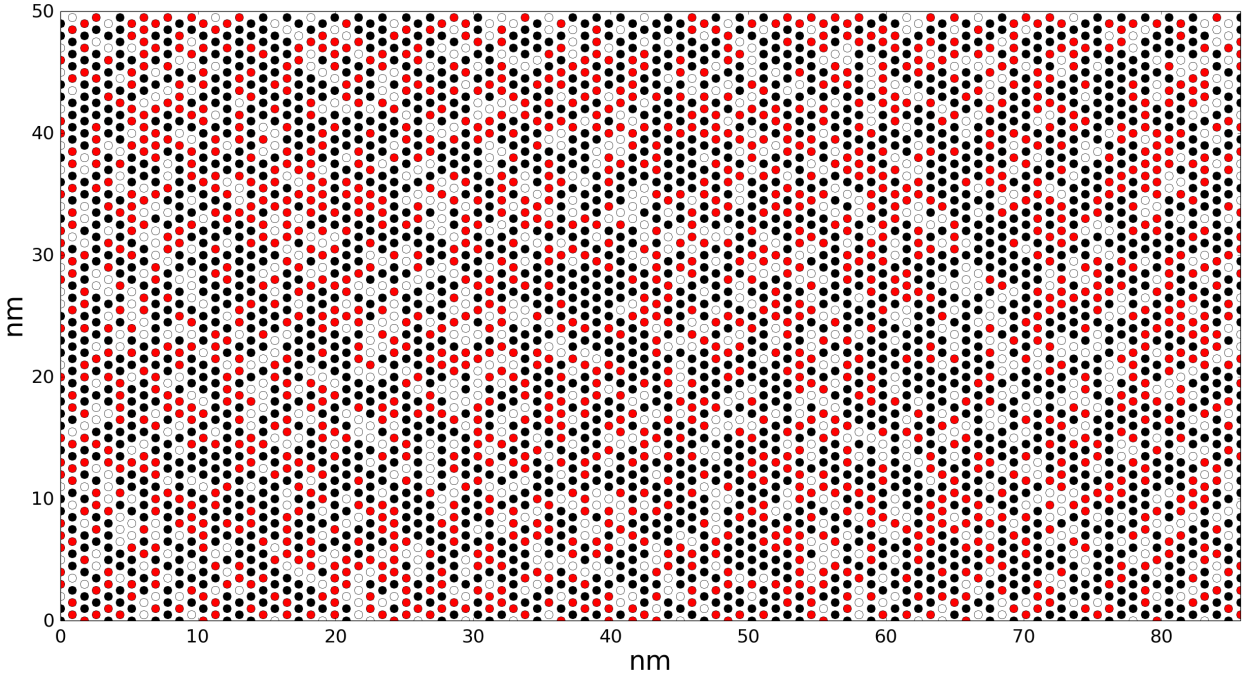

Figure S1. Snapshot of the lattice configuration at the end of a kMC simulation at steady state for $E_O = -1.0\ eV$ and $E_{CO} = -1.3\ eV$ (corresponding to the point of maximum activity in Figure 1) in the absence of lateral interactions. Red circles represent O*, black circles represent CO*.

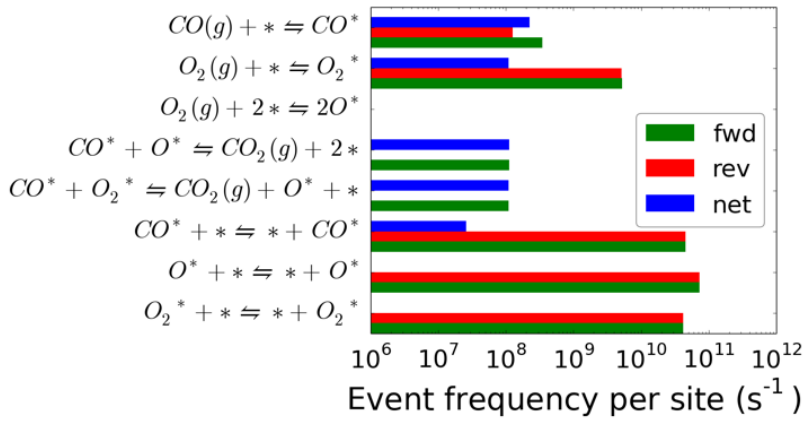

Figure S2. Event frequency for each elementary step at steady state for $E_O = -1.5\ eV$ and $E_{CO} = -1.7\ eV$ (corresponding to the point of maximum activity in Figure 5(c, d)) in the presence of lateral interactions using the parameter Set 1 in Table 1.

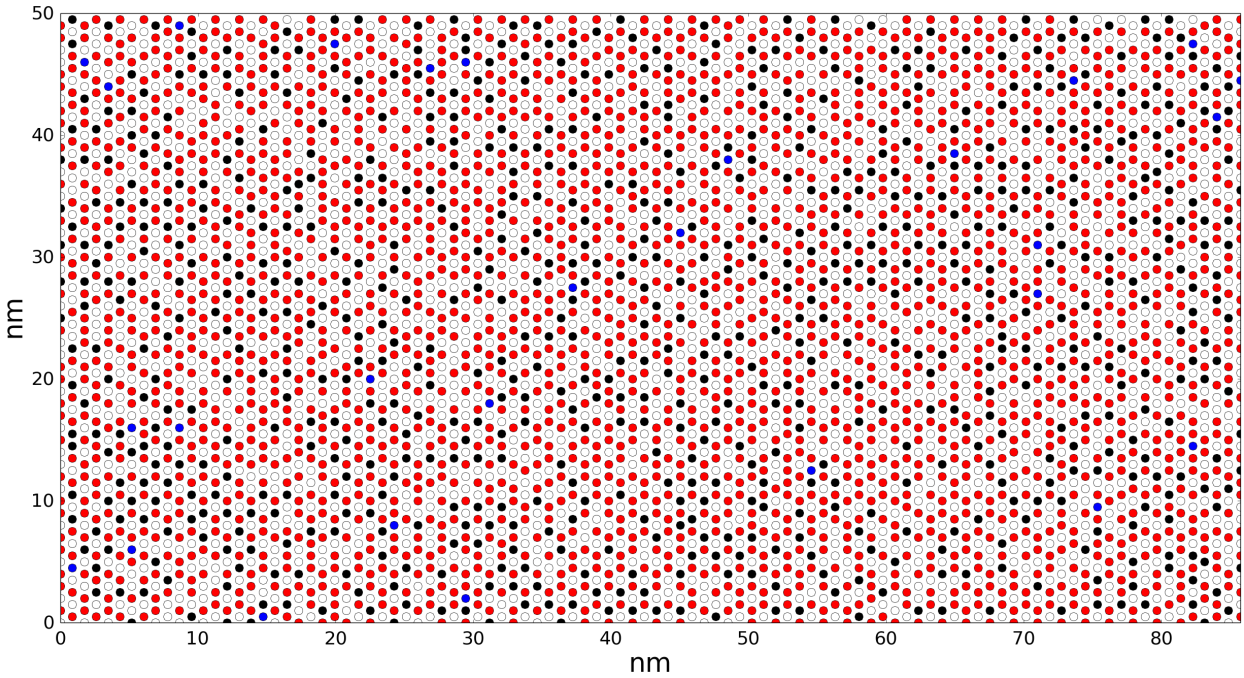

Figure S3. Snapshot of the lattice configuration at the end of a kMC simulation at steady state for $E_O = -1.5\ eV$ and $E_{CO} = -1.7\ eV$ (corresponding to the point of maximum activity in Figure 5(c, d)) in the presence of lateral interactions using the parameter Set 1 in Table 1. Red circles represent O*, blue circles represent O_2*, black circles represent CO*.

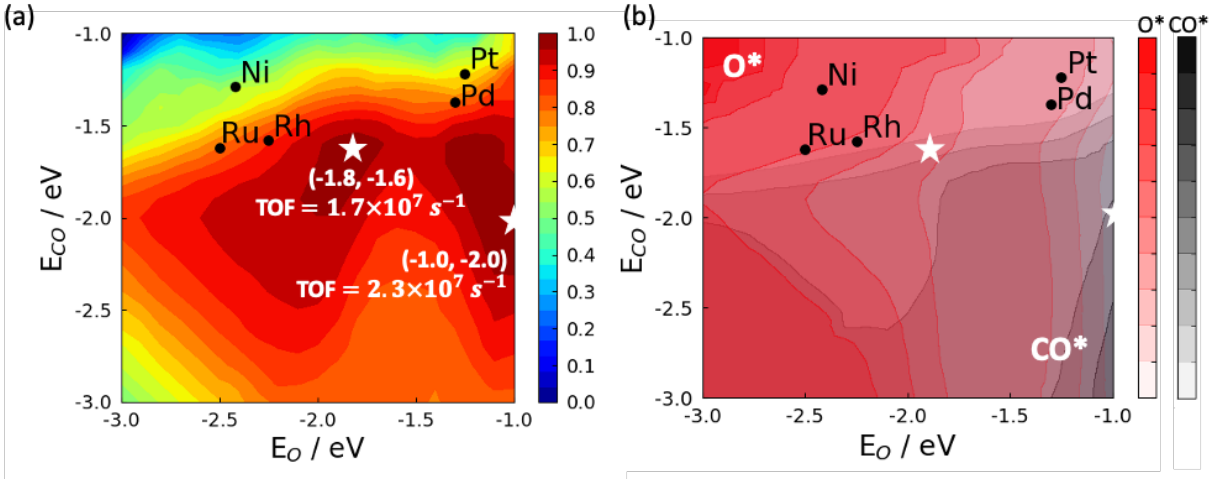

Figure S4. Trend prediction for CO oxidation as a function of E_O and E_{CO} from kMC with interaction energies from Set 1 and estimated interactions for O_2*-O_2* and O_2*-O* added at $T = 600\ K$, $P_{O_2} = 0.33\ bar$, $P_{CO_2} = 1.0\ bar$, $P_{co} = 0.67\ bar$. (a) Contour plot of the normalized TOF. (b) Corresponding surface coverages of O* (red) and CO* (black). The stars mark the points of local maximum activity and the corresponding coordinates in descriptor space are provided in parentheses. The color depth in (b) is linearly correlated with the coverage.

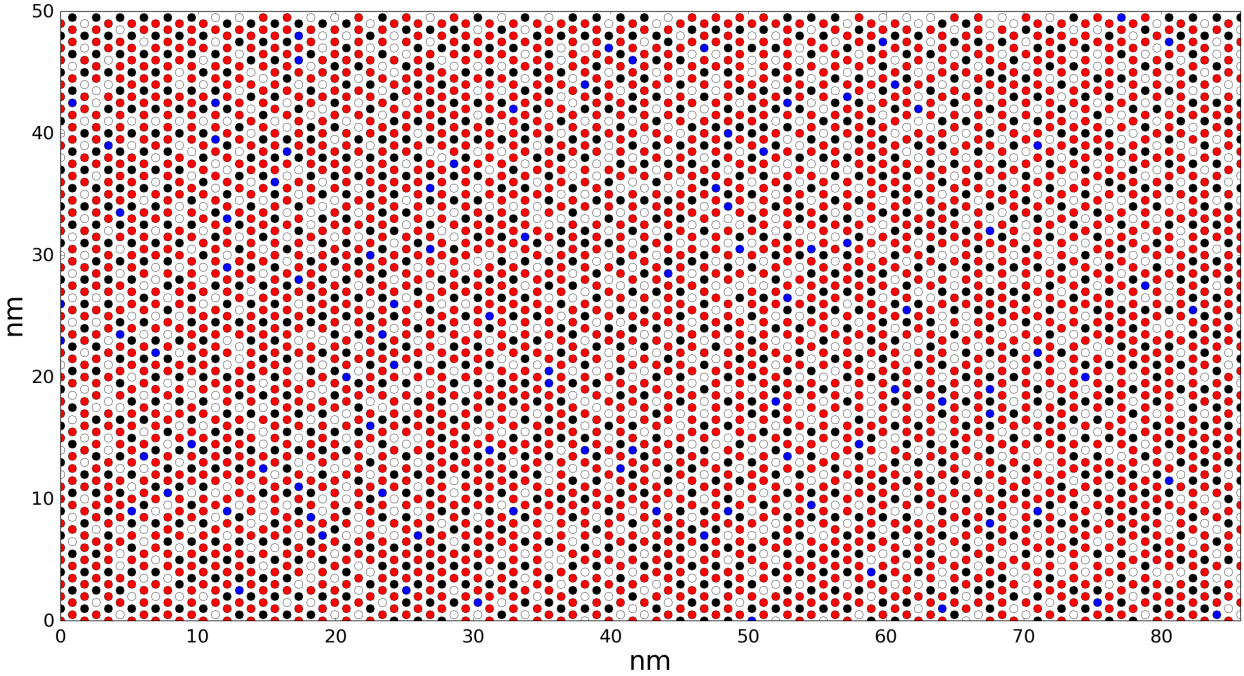

Figure S5. Snapshot of the lattice configuration at the end of a kMC simulation at steady state for $E_O = -1.6\ eV$ and $E_{CO} = -1.5\ eV$ (corresponding to the point of maximum activity in Figure 5(e, f)) in the presence of lateral interactions using the parameter Set 2 in Table 1. Red circles represent O*, blue circles represent O_2*, black circles represent CO*.

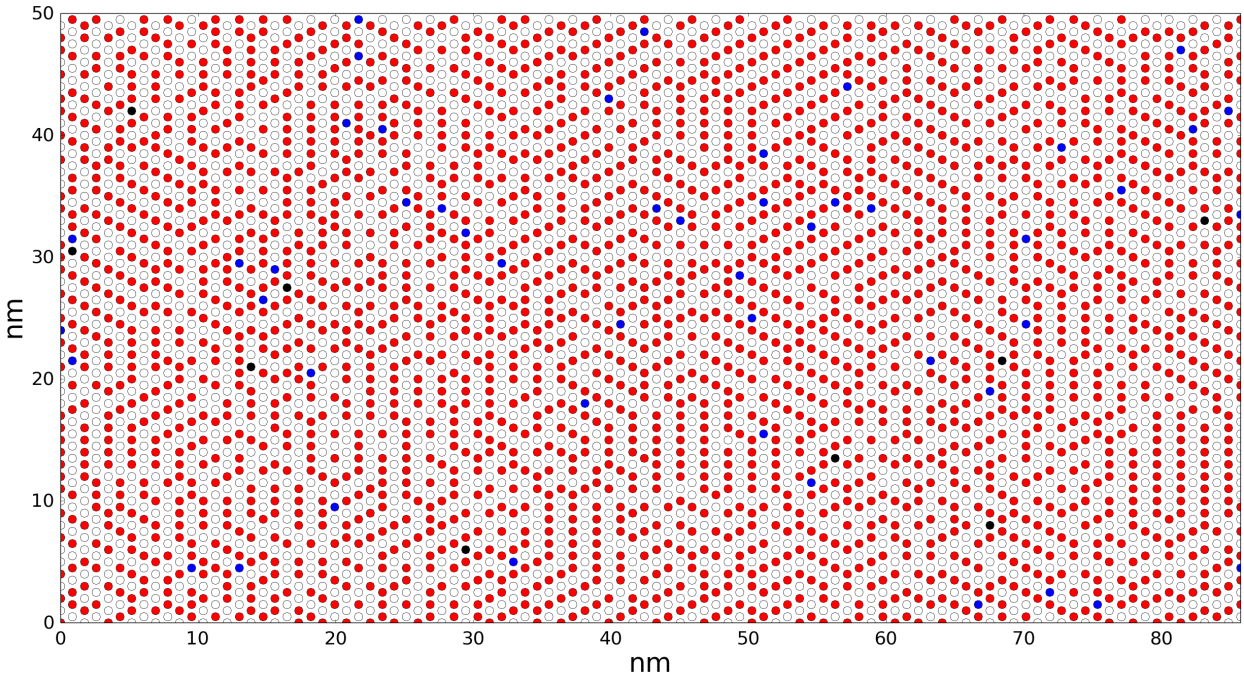

Figure S6. Snapshot of the lattice configuration at the end of a kMC simulation at steady state for $E_O = -1.5\ eV$ and $E_{CO} = -1.0\ eV$ (within the low CO*-coverage region) in the presence of lateral interactions using the parameter Set 2 in Table 1. Red circles represent O*, blue circles represent O_2*, black circles represent CO*.